Proceedings of DSCC 2019
ASME 2019 Dynamic Systems and Control Conference
October 9-11, 2019, Park City, UT, USA

DSCC2019-9029

TOWARD MAGNETO-ELECTROACTIVE ENDOLUMINAL SOFT (MEESo) ROBOTS

Jake A. Steiner[a], Omar A. Hussain[a], Lan N. Pham[b], Jake J. Abbott[b], Kam K. Leang[a*]
[a]Design, Automation, Robotics, and Control (DARC) Lab
[b]Telerobotics Lab
Department of Mechanical Engineering and the Robotics Center
University of Utah
Salt Lake City, Utah 84112

ABSTRACT

This paper introduces a magneto-electroactive endoluminal soft (MEESo) robot concept, which could enable new classes of catheters, tethered capsule endoscopes, and other mesoscale soft robots designed to navigate the natural lumens of the human body for a variety of medical applications. The MEESo locomotion mechanism combines magnetic propulsion with body deformation created by an ionic polymer-metal composite (IPMC) electroactive polymer. A detailed explanation of the MEESo concept is provided, including experimentally validated models and simulated magneto-electroactive actuation results demonstrating the locomotive benefits of incorporating an IPMC compared to magnetic actuation alone.

INTRODUCTION

The development of soft robots capable of traveling through the lumens of the human body (Fig. 1) will extend clinicians' ability to access locations deeper in the body than is currently possible, and could make current endoluminal procedures safer and/or less painful. Consider colonoscopy, which typically requires sedation to avoid discomfort, and which is often incomplete (unable to reach the cecum). There is substantial interest in robotic technologies to improve this crucial screening procedure [1,2]. Consider the insertion of catheters deep into the vasculature of the brain, which comprises narrow and complex passages that are difficult to navigate [3,4]. Conventional catheters, which are pushed from the proximal end, can be difficult to steer and control, can require multiple catheters to be inserted and extracted before reaching the desired site, and can risk perforation of the lumen. Increasing the controllability of catheters, including adding actuation at the distal end, can result in a decrease of

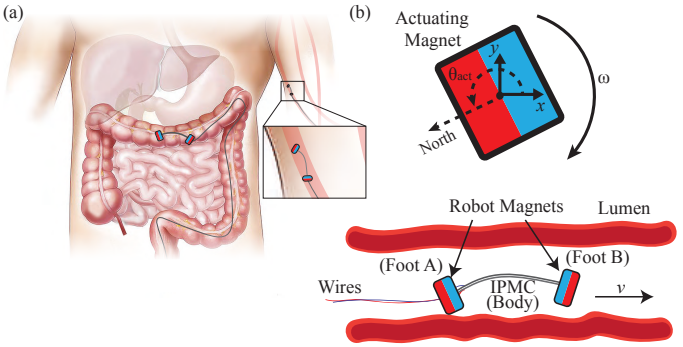

Figure 1. (a) Magneto-electroactive endoluminal soft (MEESo) robots, shown at a variety of scales traveling through natural lumens of the body (*i.e.,* intestines and blood vessels). (b) A MEESo robot comprises two magnets with opposite polarity and an ionic polymer-metal composite (IPMC) body. It is propelled by the dipole field of a rotating actuator magnet outside of the patient. Rotation ω of the actuator magnet in the direction shown results in a periodic gait in the robot that propels it with a velocity v in the direction shown; reversing ω reverses v. IPMC body deformation is used to change the shape of the robot to assist in propulsion.

*Correspondence author; e-mail: kam.k.leang@utah.edu

forces against lumen walls, and enable catheters to reach locations in the brain that are currently unreachable [5, 6].

Magneto-electroactive endoluminal soft (MEESo) robots (Fig. 1) may improve endoluminal devices. MEESo robots combine the benefits of the soft-robotic magnetic propulsion concept recently described in [7] with increased control by incorporating ionic polymer-metal composite (IPMC) actuation. MEESo robots are *continuum* robots (*i.e.,* infinite degrees of freedom), and both the magnetic and IPMC components of their actuation are forms of *intrinsic* actuation (*i.e.,* generated from within the robot itself), using the taxonomy established in [8].

The magnetic actuation alone has been experimentally shown to propel a robot, comprising two permanent magnets connected by a flexible body, through a rigid tube [7]. Rotating a dipole field, generated by either a permanent magnet or electromagnet, over the robot causes an alternating stick-slip motion. The robot is propelled forward or backward depending on the direction of rotation.

An IPMC is a soft electroactive polymer material that has the ability to actuate and sense [9–13]. Its construction involves plating an electroactive polymer (EAP), such as Nafion® (DuPont), with a conductive metal, commonly platinum or gold. Applying an electric potential across the hydrated IPMC causes deformation and bending toward the anode [14], as illustrated in Fig. 2. This deformation is caused by swelling of the polymer layer, which results from mobile hydrated cations dragging water molecules toward the cathode [12]. Flat IPMCs are typically in the range of 200–500 μm thick. As their thickness decreases, the actuation range increases. Their size, relative range of motion, versatile configuration possibilities, ability for customization and 3D printing [15], and low power requirements [11, 15], make them desirable for use in small soft robotic devices. When mechanically deformed, they generate low voltages [16], which enables them to also be used as sensors [9, 10].

The novelty of this work is the integration of an IPMC with the magnetic-propulsion method of [7]; replacing the silicone robot body with an IPMC preserves the compliance required for magnetic propulsion while permitting a controllable bias bending moment to be applied to the body of the robot, altering the static shape or dynamic gait. This paper begins with a description of the magnetic and IPMC actuation technologies that form the MEESo concept. Next, a simulation of a MEESo robot crawling in a lumen is developed, where the simulation is able to capture the making and breaking of contact between the robot and the surfaces of the lumen, and models the normal forces between the robot and the lumen. Initially, only magnetic effects are included in the simulation, and the simulation results are experimentally verified using a soft robot similar to that used in [7]. Next, the distributed bending moment of an IPMC actuator is incorporated into the simulation, and the simulation is used to explore a variety of gaits of MEESo robots in lumens. The MEESo robots rely on an inchworm gait reminiscent of that used by an "inchworm"

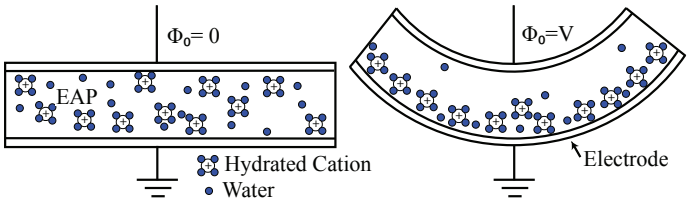

Figure 2. An ionic polymer-metal composite (IPMC) is comprised of an electroactive polymer (EAP) between two electrodes. When an electric potential, Φ_0 , is applied, the hydrated cations move toward the cathode. This motion results in a deformation curving toward the anode.

moth larvae to crawl across a surface: two feet take turns effectively anchoring to the surface of the lumen while body deformation is used to propel the robot forward. It is hypothesized that MEESo robots in other form factors may display gaits that are more reminiscent of an undulatory locomotion. The simulated results suggest that significant improvements in robot locomotion can be achieved by incorporating IPMC actuation compared to magnetic actuation alone, motivating continued research in MEESo robots.

The MEESo concept is intended to be applied to tethered capsule endoscopes and other mesoscale robots, as well as at the distal tip of catheters and endoscopes that are pushed from their proximal end, for improved performance when navigating deep into the lumens of the a human body as conceptually illustrated in Fig. 1. Magnetic methods have been applied in capsule endoscopy [1, 2, 17, 18], and both magnetic [19–22] and IPMC [23–27] catheters exist in prior work (although only a small subset have actively sought to assist in navigation through a lumen using IPMC [23]). Prior works have considered the use of magnetic fields to generate inchworm [28] and undulatory [29, 30] locomotion in lumens. However, due to the mechanical complexity of the respective designs required to generate locomotion, it is not clear how the concepts could be incorporated into a functional medical device. One study utilized SMA actuators to generate inchworm gaits in soft robots [31]. It is believed that combining magnetic and electroactive actuation will result in soft robots that will outperform those that use a single actuation method alone. Additionally, the sensing functions of an IPMC can add capabilities to the endoluminal robot beyond locomotion, enabling the design of more compact and integrated devices.

MEESo ROBOT ACTUATION PHYSICS

Two methods of actuation are combined to cause the MEESo robot to move: magnetic and electroactive. The magnetic dipole–dipole interaction between the external actuator magnet and the embedded magnets in the soft robot impose non-

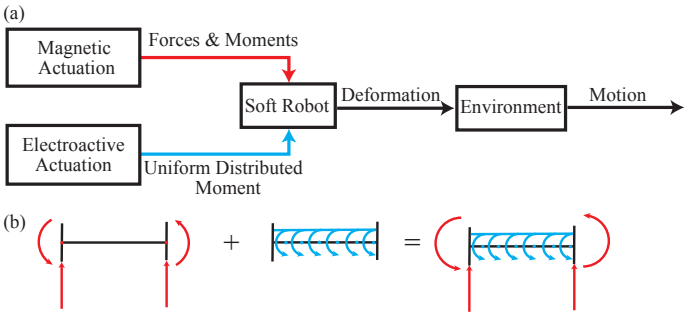

Figure 3. Process to determine the robot deformation and actuation. (a) A block diagram representing the overall system. The magnetic actuation causes forces and moments on the ends of the soft robot at the location of the embedded magnets. The electroactive actuation is achieved with an ionic polymer-metal composite (IPMC) and adds an additional bending moment across the body. Motion through the environment is achieved through cyclical body deformation. (b) The forces and moments of the IPMC and magnetic actuation are combined with superposition.

uniform forces and torques on the robot leading to actuation and deformation. The IPMC between the embedded magnets deforms the soft robot with an internal moment along the body when an electric potential is applied. A representation of the system actuation is shown in Fig. 3.

Magnetic Actuation Physics

The magnetic-actuation method was recently presented in [7]. A brief review of the method is provided here. The soft robot contains a permanent magnet embedded at each of the two ends of its body. Each of the robot's magnets can be accurately approximated by a magnetic dipole $\mathbf{m}_r$ (units A·m^2) at the center of the magnet, which points from the south pole to the north pole. The magnets are embedded in the soft robot with opposing polarity (*e.g.,* both north poles pointing outward).

The soft robot propels itself through a lumen due to the interaction of the magnets embedded in the soft robot with a single remote actuator magnet (*i.e.,* outside of the patient's body). The actuator magnet can be approximated by a magnetic dipole $\mathbf{m}_a$ (units A·m^2) at the center-of-mass of the magnet. The magnetic field $\mathbf{b}$ (units T) generated by the actuator magnet at a location $\mathbf{p}$ (units m), measured from a non-rotating frame located at the center-of-mass of the actuator magnet, is approximated by the dipole field model

$$\mathbf{b}(\mathbf{p}) = \frac{\mu_0}{4\pi||\mathbf{p}||^5}\left(3\mathbf{p}\mathbf{p}^T - I||\mathbf{p}||^2\right)\mathbf{m}_a, \tag{1}$$

where $\mu_0 = 4\pi\times10^{-7}$ T·m·A^{-1} is the permeability of free space and I is the identity matrix. The magnetic field of the actuator

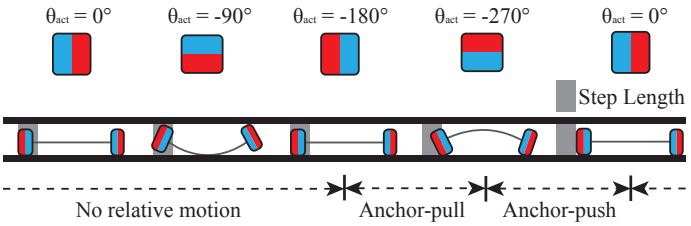

Figure 4. The magnetic soft-robot gait in a tubular environment. Simulation and experimental results both indicate an inchworm gait, with distinct anchor-pull and anchor-push phases.

magnet causes a torque $\boldsymbol{\tau}$ (units N·m)

$$\boldsymbol{\tau} = \mathbf{m}_r \times \mathbf{b} \tag{2}$$

and force $\mathbf{f}$ (units N)

$$\mathbf{f} = \nabla(\mathbf{m}_r \cdot \mathbf{b}) \tag{3}$$

on each of the robot's embedded magnets. As $\|\mathbf{p}\|$ increases, $\|\mathbf{b}\|$ and $\|\boldsymbol{\tau}\|$ decay at a rate of $\sim\|\mathbf{p}\|^{-3}$, whereas $\|\mathbf{f}\|$ decays at a rate of $\sim||\mathbf{p}||^{-4}$.

If the robot is located in a lumen with a local forward direction defined by $\hat{\mathbf{l}}$, and the actuator magnet is rotated with an angular velocity $\boldsymbol{\omega}$ (units rad·s^{-1}) in the direction of $\mathbf{p}\times\hat{\mathbf{l}}$, while keeping $\mathbf{m}_a$ orthogonal to $\boldsymbol{\omega}$, a periodic motion is induced in the soft robot, causing it to crawl forward. The sequence of the gait produced with the magnetically actuated robot is depicted in Fig. 4. It was demonstrated in [7] that both the rotating *dipole* source and embedding the magnets in the soft robot with *opposite* polarity were critical to this periodic magnetic propulsion. Using a rotating *uniform* magnetic field caused the soft robot to deform, but not to crawl in a deterministic direction. Embedding the magnets in the soft robot with the same polarity resulted in much smaller deformations in the robot, resulting in less efficient crawling. As the robot crawls farther away from the actuator magnet, the velocity will decrease until it stops due to a decrease in dipole-dipole interactions, as well as a shift in the stick-slip phases of each foot. Additionally, if the dipole actuator is located too close to the soft robot, the magnetic forces will effectively pin the robot against the environment, preventing actuating and motion.

The dipole field model Eq. (1) is perfectly accurate for spherical permanent magnets, and becomes increasingly accurate with distance for other magnet geometries, with high accuracy for certain non-spherical geometries (*e.g.,* cubes) even at relatively close distances [32]. Both permanent-magnet [33] and electromagnet [34] actuation systems have been explicitly designed to be well modeled by the dipole model of Eq. (1), and to generate a continuously rotating magnetic dipole $\mathbf{m}_a$.

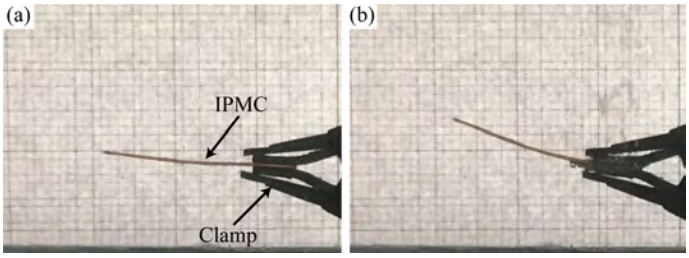

Figure 5. A cantilever IPMC deformed by an electric potential: (a) 0 V applied, (b) -3 V applied.

Electroactive Actuation Physics

An IPMC is used to bias the deflection of the electroactive body in the MEESo robot. Figure 5 demonstrates the deformation of an IPMC with applied voltage. The internal bending moment caused by the IPMC when an electric potential Φ_o is applied can be approximated as a constant moment M_{IPMC} [12]

$$M_{IPMC} \doteq k_0 \kappa_e \Phi_o a h w, \tag{4}$$

where h is half the thickness and w is the width of the IPMC, k_0 is a constitutive parameter, κ_e is the effective composite dielectric constant of the whole IPMC, and a is the inverse of the Debye length as found in [13], which is described by

$$a \doteq \sqrt{\frac{C^- \mathscr{F}^2}{\kappa_e R T}}, \tag{5}$$

Here, C^- is the anion concentration within the polymer, R is the universal gas constant, T is absolute temperature, and $\mathscr{F}$ is Faraday's constant. The effective dielectric potential of the composite consisting of the polymer and electrode is given by

$$\kappa_e = \left(\frac{2\kappa_p + \kappa_w - c(\kappa_p - \kappa_w)}{2\kappa_p + \kappa_w + c(\kappa_p - \kappa_w)} \right) \kappa_p. \tag{6}$$

The dielectric constant of water is $\kappa_w = 78\kappa_0$ and the dielectric constant of the polymer is $\kappa_p = 3\kappa_0$, where κ_0 is the permittivity of free space: $\kappa_0 = 8.85 \times 10^{-12}$ F·m^{-1}. Lastly, the volume fraction of water inside the polymer layer c can be found from

$$c = \frac{4\pi r_c^3}{3 r_d^3}, \tag{7}$$

where r_d is the mean distance between groups or clusters of sulfonate from the Nafion backbone, and r_c is the radius of each cluster.

MEESo ROBOT GAIT SIMULATION

The simulation of the MEESo robot reduces to a 2D model. All the forces are in the xy-plane and the moments are purely in the z-direction. When the body of the robot deforms, the feet move relative to the environment. Which foot-contact point moves and which foot it stationary during a phase of the gait is determined by the reaction forces at the points of contact with the environment. The sequences of motion caused by the magnetic dipole-dipole interactions and the IPMC creates motion through the lumen. A model of the effects of the magnetic interaction and gravity is first presented and validated with experiments. Superposition is then used to add the effects of the IPMC actuation to the model.

Magnetic Gait Simulation

The simulated magnetic actuation is presented first. For simulation, the geometry of the robot is simplified. The body is represented as a deformable beam with one-dimensional rigid feet connected perpendicular at the end of the body on both sides. The lumen environment is simplified to a rigid ceiling and floor. The setup of the simulation is shown in Fig. 6. The dipole-dipole interactions (forces and torques) on all robot magnets are considered, the weight of the body is represented as a distributed load, and the weight of the feet are represented as point loads on the ends of the beam. When determining the body deformation, only forces along the y-direction are considered, and it is assumed the forces along the y-direction are much greater then the forces along the x-direction.

To determine the locomotion of the soft robot, the deformation of the robot under static equilibrium is found for the current angle of the actuator magnet. By successively cycling through discretized actuator-dipole angles and determining the static equilibrium with proper constraints, the motion of the robot is determined.

To solve for the static equilibrium of the system, an iterative approach is used. To determine the deformation of the robot body with the given forces and moments, the robot is represented as a beam supported by roller supports. The surfaces of the environment are only capable of reaction forces that push on the robot. The support locations are iteratively moved until the reaction forces satisfy the environmental constraints: the reaction forces are either perpendicular away from the surface or zero. The following equation is how the support location for foot A, A^i_{Sy}, of the current iteration i, is vertically moved for the next iteration $(i+1)$ based off the reaction force F_{AR} at A^i_{Sy}:

$$A'_{Sy} = -kF_{AR} + A^i_{Sy} \tag{8}$$

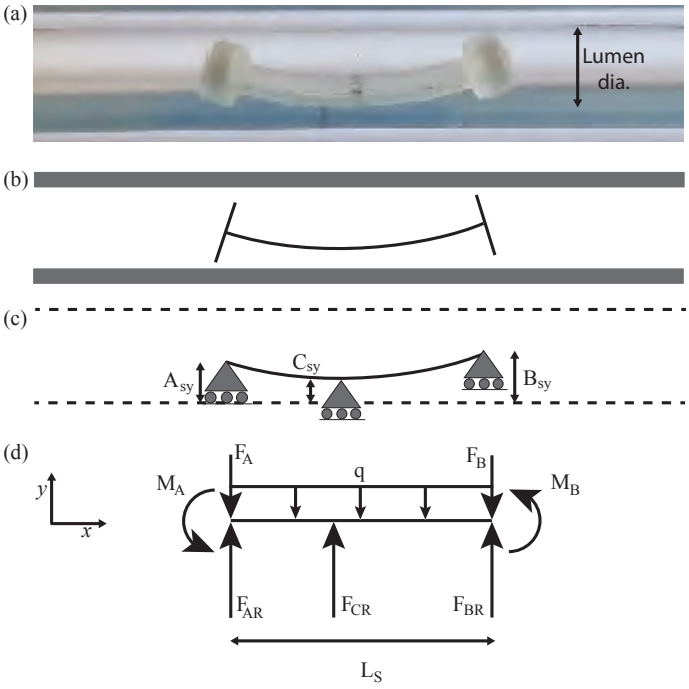

Figure 6. The robot simulation simplifies the geometry of the robot into a beam with roller supports. (a) A photo of the magnetically actuated soft robot described in [7]. (b) The simplified geometry of the robot represented in the simulation environment. The feet are point contacts, and the body is a deformable beam. (c) The statics problem with support location constraints shown as roller supports. (d) The free-body diagram showing the forces and moments: the weight of the body is considered as a distributed load q across the support-separation distance L_s, the weight of the magnets and the vertical components of the forces between the magnets (actuator magnet and respective robot magnet) are included in F_A and F_B, and the reaction forces at the feet contact points are included in F_{AR} and F_{BR}. The moments caused by the actuator magnet and the respective robot magnet are included in M_A and M_B.

and

$$A_{Sy}^{i+1} = \begin{cases} \text{floor}, & \text{if } A'_{Sy} - d_{foot} < \text{floor} \\ \text{ceiling}, & \text{if } A'_{Sy} + d_{foot} > \text{ceiling} \\ A'_{Sy}, & \text{otherwise}, \end{cases} \tag{9}$$

where k determines how much the support moves after each iteration, and d_{foot} is the vertical distance from the middle of the foot to the end of the foot (which is a function of the current angle of the foot). Equations (8) and (9) are repeated for points B and C. If C is not touching a surface, then it does not need to be considered a constraint in the static problem. When solving for beam deflection, the simulation is simplified by assuming that the reaction forces on the feet, due to contact with the surfaces, are equivalent to the force on the end of the body. When calculating the beam displacement, two scenarios are considered: (1) if the body is touching, then the beam has three support locations A_{Sy}, B_{Sy} and C_{Sy} and (2) if the center is not touching then there are two support locations A_{Sy} and B_{Sy}. A free-body diagram of the soft robot is shown in Fig. 6(d). It is assumed that the foot with the greater reaction force has a higher friction force and remains stationary relative to the environment between iterations. Friction's effect on the deformation of the beam is not considered.

To correct for the length of the beam when deformed, the support separation length L_s^i is adjusted. If the deformed beam length L is greater than the true length of the beam L_T, then L_s is reduced by δ (δ can be a small length or defined as $\delta = |L_T - L|$). If the deformed beam is shorter than the true length, then L_s is increased by δ. Length L_s for the next iteration is found with the following equation

$$L_s^{i+1} = L_s^i + \begin{cases} \delta, & \text{if } L_T < L \\ -\delta, & \text{if } L_T > L \\ 0, & \text{otherwise.} \end{cases} \tag{10}$$

Once the static equilibrium has converged for a given actuator-angle θ_{act}, the locations of the contact points of the feet are saved to be used as constraints for the next actuator angle. A number of the iteration variables could be used for convergence. The author defines convergence when the sum of the change in discretized beam locations from iteration $i-1$ to i are less then a small number. At each iteration step, after the robot's deformation is determined, the robot's location within the environment is determined based on the previous actuator angle. The foot location with the higher reaction force is fixed to the location in the environment based on the solution for the prior actuation angle. The position of the rest of the beam can be found after this point is fixed. In the case of both feet not touching a surface (*i.e.,* the robot in a "U" shape), it is assumed that the beam does not move relative to the center location of the beam.

The iteration process to determine the static equilibrium at θ_{act} is shown graphically in Fig. 7. It depicts the motion of the support locations, the change in the length of the beam, and the placement in the environment. Notice that the support on foot B, the right foot, moved until the reaction force satisfies the assigned constraints. Since the foot is not touching a surface, the reaction force must be zero. Figure 8 shows the iteration variables for the robot at a given actuator angle. Foot B moves toward the ceiling. The support location B_{Sy} moves up, and the reaction force at B goes from negative to near zero. The contact point of foot A (the left foot) remains fixed during the iteration due to the reaction force on foot A being higher than that on foot B. The separation of the supports L_s is shown and converges on a value such that $L = L_T$. The algorithm for robot motion is provided in Alg. 1.

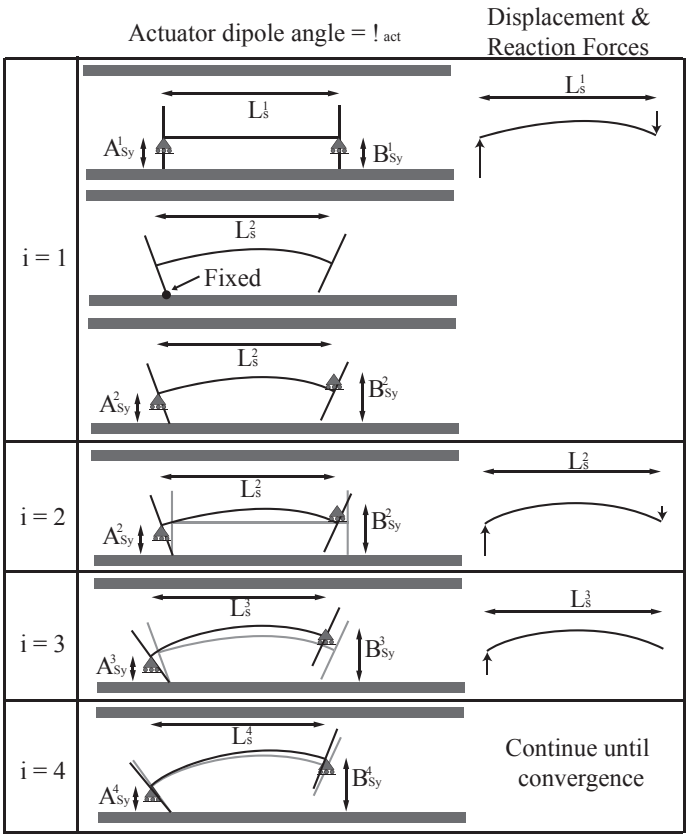

Figure 7. Iteration process graphically shown for converging on the static equilibrium. The support locations are moved until the roller constraints are met. Foot B (right foot) moves up until the constraints are satisfied. Foot A (left foot) stays stationary between the iterations because the reaction force is higher.

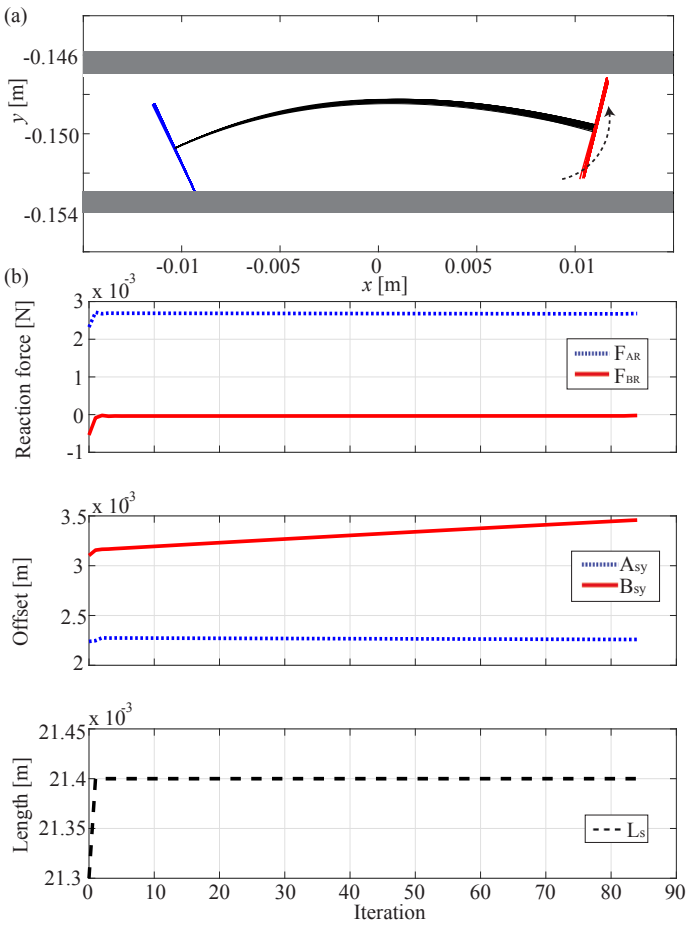

Figure 8. The variables for static equilibrium for a given constant actuator angle θ_{act}. The actuator magnet is located at [0, 0]. (a) Robot deformations for all iterations superimposed. The left foot remains stationary between iterations because the reaction force is higher. (b) The reaction force, support offsets, and support separation change are shown.

Experimental Validation of Magnetic Gait Simulation

The magnetic gait simulation is experimentally validated using a soft robot similar, to the experiments described in [7]. A robot with a deformable silicone body, shown in Fig. 9, was tested and compared to the simulation results. The actuator-magnetic dipole was set to 80 A·m^2, the robot magnet strength is 0.011 A·m^2, the distance to the robot is 0.133 m, the tube diameter is 12 mm, the total weight of the robot is 0.437 g, and the feet are 0.5 mm wide and 10 mm in diameter. The robot was manufactured with thin feet to reduce the possible effect caused by the thickness of the feet, as it is not considered in the simulation. The simulated soft robot traveled at a speed of 12.0 mm/rev, and the physical soft robot traveled at 11.6 mm/rev. In addition, the gait of the simulated and physical robots were qualitatively the same: there is an anchor-pull phase in which the front-foot point of contact remained constant and the back foot slipped along the surface toward the front foot, followed by an anchor-push phase in which the back foot did not slip and the front foot was pushed forward, away from the back foot.

A second soft robot, like the one shown in Fig. 6(a), 25 mm long with 3 mm thick feet, was tested at a distance of 0.153 m from the actuator magnet dipole of strength 80 A·m^2 in a tube diameter of 6 mm. The simulation speed was 4.05 mm/rev and the physical soft robot traveled at 1.8 mm/rev. The timing of the gait phases was the same, but the width of the feet caused the physical robot to travel more slowly than the simulation. The strength of the actuator dipole was then reduced to 40 A·m^2. The simulation predicted 3.1 mm/rev and the physical robot moved at 0.5 mm/rev. As the forces and moments of the magnetic field reduce, friction has a more significant effect on the crawling motion of the robot. The simulation does not take into account friction's effects on the deformation of the body and is only considered when determining which foot anchors during the iterations.

Algorithm 1: Determine motion of soft robot

Initialize: environment, beam location, and mechanical parameters
for $\theta_{act} = \theta_{act}^{initial} \rightarrow \theta_{act}^{final}$ **do**
  Save initial contact points where the robot touches the environment
  for *i = 0 to m* ***or*** *convergence* **do**
    Determine torques and forces on robot magnets: Eq. (2) & Eq. (3)
    Determine which point is fixed in the environment
    Solve for the beam displacement, robot geometry, and reaction forces: F_{AR}, F_{CR}, and F_{BR}
    Find L_s^{i+1} with Eq. (10)
    Determine A_{Sy}^{i+1}, C_{Sy}^{i+1} and B_{Sy}^{i+1}: Eq. (8) & Eq. (9)
    Check for convergence
  end
  Increment θ_{act}
end

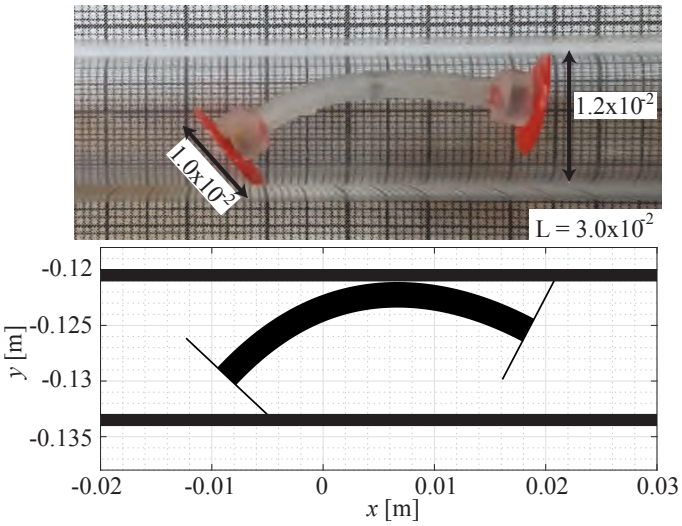

Figure 9. The magnetically actuated soft robot with a silicone body and thin plastic feet matched closely to the simulation. The actuator magnet is located at [0, 0] and all units are in meters.

Complete MEESo Gait Simulation

In this section, the effect of the IPMC actuation is incorporated (*i.e.,* superimposed) into the existing simulation to create a complete simulation for the MEESo robot. The soft robot's body is replaced with an IPMC actuator. The IPMC, with an applied voltage, will add a distributed moment to the deformable body given by Eq. (4). The total moment along the body, M_t, is found by adding the moments caused by the magnetic actuation M_{mag} to the moments caused by the IPMC, M_{IPMC}, using superposition. The displacement of the curve, $w(x)$, is found by double integration of

$$w'' = \frac{M_t}{EI}, \tag{11}$$

where E is the Young's Modulus of the body, I is the area moment of inertia about the neutral axis, and $M_t = M_{mag} + M_{IPMC}$ is the total moment along the length of the beam. Integration constants are found using boundary conditions at the support locations.

MEESo SIMULATION RESULTS AND DISCUSSION

The effects of adding IPMC actuation to the magnetic soft robot were simulated next. The dimensions of the soft robot and environment were kept constant for all simulations.The actuator dipole strength was $80\,\mathrm{m{\cdot}A^2}$, the robot magnet strength was $0.011\,\mathrm{A{\cdot}m^2}$, the foot diameter was 10 mm, the length was 30 mm, and the IPMC body was $200\,\mu$m thick and 3.3 mm wide. The values used for Eqs. (4), (5), (6), and (7) to determine the IPMC moment are $r_c = 10$ Å, $r_d = 22.2$ Å, $C^- = 1070\,\mathrm{mol{\cdot}m^{-3}}$, $k_0 = 21\,\mathrm{J{\cdot}C^{-1}}$, and ϕ_o is the applied voltage.

The first simulation looked at the effect of a constant voltage being applied to the IPMC. A positive voltage causes the middle to raise (*i.e.,* form an arch) and a negative voltage causes the middle to lower (*i.e.,* form a "U"). The simulations were all run with the actuator magnet remaining at the [0, 0] location. The actuator magnet was rotated clockwise through 30 rotations. Figure 10 shows the simulation results for the MEESo robot. The velocity of the simulated soft robots are shown in Fig. 10(b) and (c) as they move along the tube in the positive x-direction. It can be seen in Fig. 10(b) that a constant positive voltage increased the velocity of the robot, whereas a negative voltage reduced it. The benefit of a positive voltage has a diminishing return with increasing voltages. This is because the deformation of the body of the robot is constrained by the height of the tube. A negative voltage retards the anchor-push phase of the gait and causes the soft robot to take smaller steps.

Next, a sinusoidal actuation of the IPMC was tested at different phase shifts from the actuator magnet angular rotation. Sinusoidal waves of the same frequency as the actuator magnet rotation with an amplitude of 2 V were tested. As the soft robot traveled through the tube in the positive x-direction, the different phase shifts had a significant effect on the velocity. For example, at $x = 0.10$ m, with no electroactive actuation the soft robot was traveling approximately 4 mm/rev, and with an applied voltage $V = 2\sin(\theta_{act} + 0.5\pi)$ this velocity was increased to approximately 7.0 mm/rev. It also appears that the optimal phasing is a function of the location of the MEESo robot with respect to the actuator magnet.

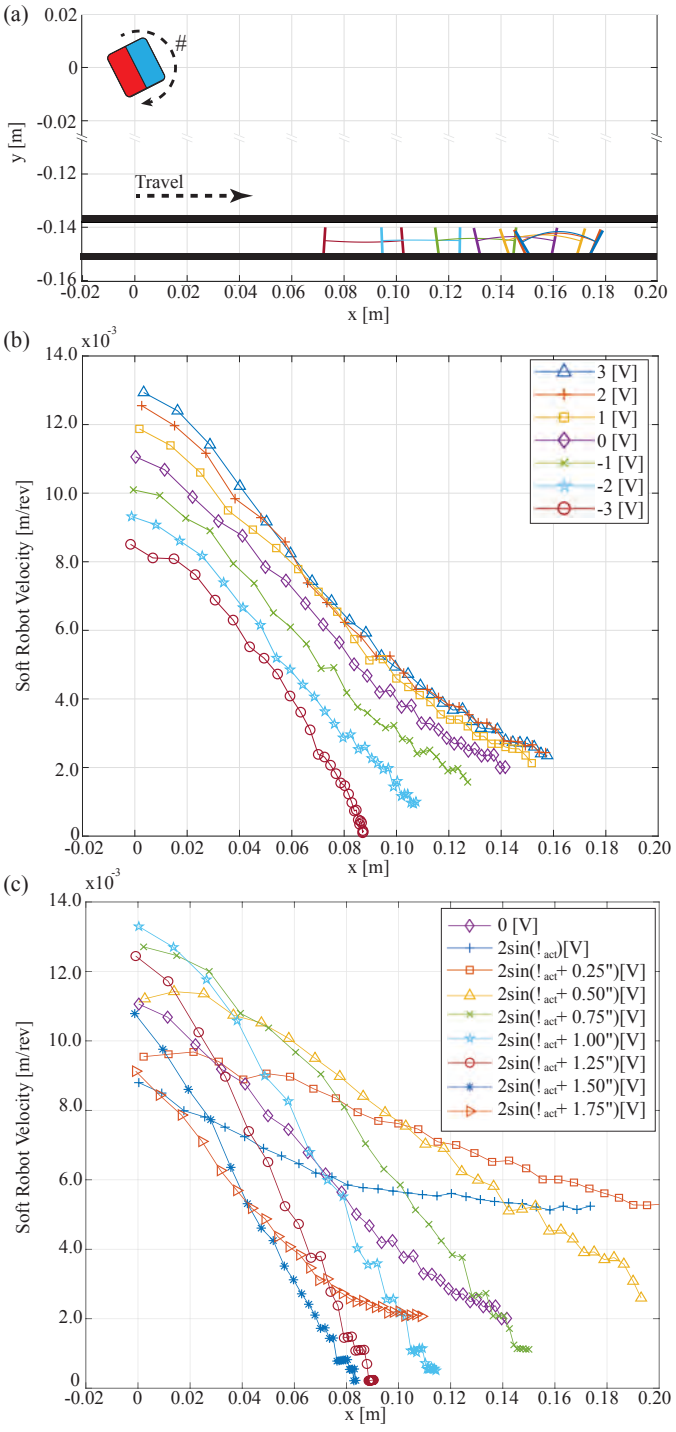

Figure 10. Simulation results for a MEESo robot under different IPMC excitations. The actuator magnet's position is stationary at [0, 0]. The robots all started at $x = 0$, the actuator magnet rotated clockwise, and the robots traveled to the right. (a) Shows the progress of the robots after 30 revolutions of the actuator magnet for seven simulations, each with a different constant voltage applied to the ionic polymer-metal composite body, corresponding to (b). (c) The velocity of the MEESo robot with different sinusoidal voltages.

CONCLUSION AND FUTURE WORK

A magneto-electroactive endoluminal soft (MEESo) robot combines the actuation of an electroactive polymer (IPMC) with magnetic propulsion generated by a rotating dipole field. The IPMC adds an additional bending moment to the body of the soft robot and can change the gait to improve performance over magnetic propulsion alone. A model for the MEESo robot was created and validated with comparison to experimental results. Simulation results show the possible locomotive benefits by incorporating electroactive actuation into the soft robot's actuation.

Future work primarily involves fabricating MEESo robot prototypes and testing them with magneto-electroactive actuation. This will include experimental confirmation of the effects of the electroactive actuation phase shift and voltage changes described herein. From there, modifications to the IPMC geometry can be considered, including incorporation of additional degree of freedom beyond simple locomotion. To further increase the complexity of the IPMC geometry, additive manufacturing techniques will be considered.

ACKNOWLEDGEMENT

This work was supported by the National Science Foundation under under grant numbers 1830958 and 1545857.

REFERENCES

[1] Sliker, L. J., and Ciuti, G., 2014. "Flexible and capsule endoscopy for screening, diagnosis and treatment". *Expert Rev. Med. Devices,* **11**(6), pp. 649–666.

[2] Ciuti, G., Caliò, R., Camboni, D., Neri, L., Bianchi, F., Arezzo, A., Koulaouzidis, A., Schostek, S., Stoyanov, D., Oddo, C. M., Magnani, B., Menciassi, A., Morino, M., Schurr, M. O., and Dario, P., 2016. "Frontiers of robotic endoscopic capsules: a review". *J. Microbio. Robot.,* **11**(1–4), pp. 1–18.

[3] Novitzke, J., 2009. "A patient guide to brain stent placement.". *J. Vasc. Interv. Neurol.,* **2**(2), pp. 177–179.

[4] Histed, M. H., Bonin, V., and Reid, R. C., 2009. "Direct activation of sparse, distributed populations of cortical neurons by electrical microstimulation". *Neuron,* **63**(4), pp. 508–522.

[5] Jayender, J., Patel, R. V., and Nikumb, S., 2009. "Robot-assisted active catheter insertion: Algorithms and experiments". *Int. J. Robot. Res.,* **28**(9), pp. 1101–1117.

[6] Fu, Y., Liu, H., Huang, W., Wang, S., and Liang, Z., 2009. "Steerable catheters in minimally invasive vascular surgery". *Int. J. Med. Robot. Comp.,* **5**(4), pp. 381–391.

[7] Pham, L. N., and Abbott, J. J., 2018. "A soft robot to navigate the lumens of the body using undulatory locomotion generated by a rotating magnetic dipole field". In Proc. IEEE/RSJ Int. Conf. Intell. Robot. Syst., pp. 1783–1788.

[8] Burgner-Kahrs, J., Rucker, D. C., and Choset, H., 2015.

"Continuum robots for medical applications: A survey". *IEEE Trans. Robotics,* **31**(6), pp. 1261–1280.

[9] Aureli, M., and Porfiri, M., 2013. "Nonlinear sensing of ionic polymer metal composites". *Continuum Mechanics and Thermodynamics,* **25**(2-4), pp. 273–310.

[10] Bonomo, C., Brunetto, P., Fortuna, L., Giannone, P., Graziani, S., and Strazzeri, S., 2008. "A tactile sensor for biomedical applications based on IPMCs". *IEEE Sensors Journal,* **8**(8), pp. 1486–1493.

[11] Carrico, J. D., Tyler, T., and Leang, K. K., 2018. "A comprehensive review of select smart polymeric and gel actuators for soft mechatronics and robotics applications: Fundamentals, freeform fabrication, and motion control". *Int. J. Smart and Nano Materials,* **8**(4), pp. 144–213.

[12] Nemat-Nasser, S., and Li, J. Y., 2000. "Electromechanical response of ionic polymer-metal composites". *J. Appl. Phys.,* **87**(7), pp. 3321–3331.

[13] Porfiri, M., Leronni, A., and Bardella, L., 2017. "An alternative explanation of back-relaxation in ionic polymer metal composites". *Extreme Mech. Lett.,* **13**, pp. 78–83.

[14] Cha, Y., and Porfiri, M., 2014. "Mechanics and electrochemistry of ionic polymer metal composites". *Journal of the Mechanics and Physics of Solids,* **71**(1), pp. 156–178.

[15] Carrico, J. D., Traeden, N. W., Aureli, M., and Leang, K. K., 2015. "Fused filament 3D printing of ionic polymer-metal composites (IPMCs)". *Smart Mater. Struct.,* **24**(12), p. 125021.

[16] Aureli, M., Prince, C., Porfiri, M., and Peterson, S. D., 2010. "Energy harvesting from base excitation of ionic polymer metal composites in fluid environments". *Smart Mater. Struct.,* **19**(1), p. 015003.

[17] Mahoney, A. W., and Abbott, J. J., 2014. "Generating rotating magnetic fields with a single permanent magnet for propulsion of untethered magnetic devices in a lumen". *IEEE Trans. Robot.,* **30**(2), pp. 411–420.

[18] Popek, K. M., Hermans, T., and Abbott, J. J., 2017. "First demonstration of simultaneous localization and propulsion of a magnetic capsule in a lumen using a single rotating magnet". In Proc. IEEE Int. Conf. Robot. Autom., pp. 1154–1160.

[19] Ernst, S., Ouyang, F., Linder, C., Hertting, K., Stahl, F., Chun, J., Hachiya, H., Bänsch, D., Antz, M., and Kuck-Heinz, K., 2004. "Initial experience with remote catheter ablation using a novel magnetic navigation system: magnetic remote catheter ablation". *Circulation,* **109**(12), pp. 1472–1475.

[20] Pappone, C., Vicedomini, G., Manguso, F., Gugliotta, F., Mazzone, P., Gulletta, S., Sora, N., Sala, S., Marzi, A., Augello, G., Livolsi, L., Santagostino, A., and Santinelli, V., 2006. "Robotic magnetic navigation for atrial fibrillation ablation". *J. Am. Coll. Cardiol.,* **47**(7), pp. 1390–1400.

[21] Kratchman, L. B., Bruns, T. L., Abbott, J. J., and Webster III, R. J., 2017. "Guiding elastic rods with a robot-manipulated magnet for medical applications". *IEEE Trans. Robot.,* **33**(1), pp. 227–233.

[22] Edelmann, J., Petruska, A. J., and Nelson, B. J., 2017. "Magnetic control of continuum devices". *Int. J. Robot. Res.,* **36**(1), pp. 65–85.

[23] Ali, A., Plettenburg, D. H., and Breedveld, P., 2016. "Steerable catheters in cardiology: Classifying steerability and assessing future challenges". *IEEE Transactions on Biomedical Engineering,* **63**(4), April, pp. 679–693.

[24] Fang, B. K., Ju, M. S., and Lin, C. C. K., 2007. "A new approach to develop ionic polymer-metal composites (IPMC) actuator: Fabrication and control for active catheter systems". *Sens. Actuators A: Phys.,* **137**(2), pp. 321–329.

[25] Ruiz, S., Mead, B., Palmre, V., Kim, K. J., and Yim, W., 2015. "A cylindrical ionic polymer-metal composite-based robotic catheter platform: Modeling, design and control". *Smart Mater. Struct.,* **24**(4).

[26] Yoon, W. J., Reinhall, P. G., and Seibel, E. J., 2007. "Analysis of electro-active polymer bending: a component in a low cost ultrathin scanning endoscope". *Sens. Actuators A: Phys.,* **133**(2), pp. 506–517.

[27] Rasmussen, L., Bahramzadeh, Y., and Shahinpoor, M., 2012. "Electroactivity in polymeric materials". In *Electroactivity in Polymeric Materials*, L. Rasmussen, ed. Springer, ch. Chapter 2, pp. 57–65.

[28] Kim, S. H., Hashi, S., and Ishiyama, K., 2013. "Hybrid magnetic mechanism for active locomotion based on inchworm motion". *Smart Mater. Struct.,* **22**, p. 027001.

[29] Nam, J., Jeon, S., Kim, S., and Jang, G., 2014. "Crawling microrobot actuated by a magnetic navigation system in tubular environments". *Sens. Actuators A: Phys.,* **209**, pp. 100–106.

[30] Nam, J., Jang, G. H., Jeon, S. M., and Jang, G. H., 2014. "Development of a crawling microrobot with high steering capability and high stability to navigate through a sharply bent tubular environment". *IEEE Trans. Magn.,* **50**(11), p. 8500704.

[31] Wang, W., Lee, J., Rodrigue, H., Song, S., Chu, W., and Ahn, S., 2014. "Locomotion of inchworm-inspired robot made of smart soft composite (SSC)". *Bioinspir. Biomim.,* **9**, p. 046006.

[32] Petruska, A. J., and Abbott, J. J., 2013. "Optimal permanent-magnet geometries for dipole field approximation". *IEEE Trans. Magn.,* **49**(2), pp. 811–819.

[33] Wright, S. E., Mahoney, A. W., Popek, K. M., and Abbott, J. J., 2017. "The spherical-actuator-magnet manipulator: A permanent-magnet robotic end-effector". *IEEE Trans. Robot.,* **33**(5), pp. 1013–1024.

[34] Petruska, A. J., and Abbott, J. J., 2014. "Omnimagnet: An omnidirectional electromagnet for controlled dipole-field generation". *IEEE Trans. Magn.,* **50**(7), p. 8400810.